Supporting Information

Setting the sequence of slicing events along deep subduction interfaces: 2. *P-T* conditions and timing of accretion and exhumation in western Crete (Hellenic margin)

Armel Menant[1,2*], Johannes Glodny[2], Samuel Angiboust[3,4], Edward R. Sobel[5], Eloïse Bessière[1], Laurent Jolivet[6], Romain Augier[7], Onno Oncken[2]

[1] Université Côte d'Azur, CNRS, Observatoire de la Côte d'Azur, IRD, Géoazur, Valbonne, France

[2] GFZ Helmholtz Centre Potsdam, German Research Centre for Geosciences, Potsdam, Germany

[3] École Normale Supérieure of Lyon, Université de Lyon, LGL-TPE, Lyon, France

[4] Institut Universitaire de France (IUF), Paris, France

[5] Institute of Geosciences, Universität Potsdam, Potsdam-Golm, Germany

[6] Sorbonne Université, CNRS-INSU, Institut des Sciences de la Terre de Paris (ISTeP), UMR7193, Paris, France

[7] Université d'Orléans, CNRS, BRGM, Institut de Sciences de la Terre d'Orléans (ISTO), UMR7327, Orléans, France

[*] Corresponding author (email: armel.menant@geoazur.unice.fr)

Table S1: Summary of petrological observations, chemical characteristics of key H*P*/L*T* minerals and *Rb*/*Sr* ages for all the samples from the H*P*-L*T* units. Samples with an asterisk (*) are presented in Supporting Information only. *i.d.*: Isotopic disequilibrium.

Sample	Tectono-metamorphic unit	Latitude	Longitude	Main paragenesis	Si^{4+} (Ph, pfu)	X_{Mg} (Cph)	X_{Mg} (Cld)	X_{Mg} (Chl)	Rb/Sr age (Ma)
CR2039	High-*T* Phyllite-Quartzite	35°32’18’’N	23°43’38’’E	Chl, Ep, Ph, Pg, Qz, Cal	3.19-3.29			0.45-0.47	16.4 ± 1.6
CR1965b	Medium-*T* Phyllite-Quartzite	35°21’12’’N	23°48’45’’E	Cld, Ph, Pg, Chl, Qz	3.28-3.39		0.06-0.07	0.28-0.32	20.8 ± 1.4
CR1925a	Medium-*T* Phyllite-Quartzite	35°18’09’’N	23°41’45’’E	Ph, Pg, Dol, Qz	3.09-3.18				24.3 ± 1.2
CR1935b	Medium-*T* Phyllite-Quartzite	35°22’42’’N	23°54’04’’E	Chl, Ph, Pg, Ab, Qz, Dol, Cal	3.34-3.42			0.52-0.54	15.75 ± 0.55
CR1920b	Upper Trypali	35°16’57’’N	23°37’37’’E	Lws, Ph, Pg, Qz, Dol	3.23-3.37				19.04 ± 0.76
CR1957b	Upper Trypali	35°17’30’’N	23°47’08’’E	Cal, Ph, Qz	3.17-3.24				16.59 ± 0.25
CR2073	Upper Trypali	35°16’13’’N	23°44’36’’E	Cal, Ph, Qz	3.09-3.13				16.74 ± 0.37
CR1917b	Upper Trypali	35°16’28’’N	23°36’43’’E	Car, Ph, Pg, Qz, Arg, Dol	3.28-3.32	ca. 0.80			14.66 ± 0.68
CR1945d	Upper Trypali	35°17’06’’N	23°41’35’’E	Car, Ph, Pg, Qz, Dol	3.22-3.26	0.71-0.74			15.5 ± 1.2
CR1945b (vein)	Upper Trypali	35°17’06’’N	23°41’35’’E	Lws, Ph, Pg, Chl, Qz, Dol	3.20-3.25			0.77-0.79	17.02 ± 0.50
CR1945b (host)	Upper Trypali	35°17’06’’N	23°41’35’’E	Ph, Dol	3.21-3.27				16.1 ± 4.6
CR2055b	Plattenkalk *s.l.*	35°19’47’’N	23°57’10’’E	Ph, Chl, Cal, Qz	3.28-3.41			0.46-0.54	41.79 ± 0.66
CR1902b*	High-*T* Phyllite-Quartzite	35°30’14’’N	23°44’09’’E	Cld, Ph, Pg, Qz	3.08-3.13		0.10-0.11		*i.d.*
CR1918a*	Upper Trypali	35°16’51’’N	23°37’21’’E	Lws, Ph, Pg, Chl, Qz, Dol	3.17-3.24			0.99-1.00	31.9 ± 3.3
CR2055a*	Plattenkalk *s.l.*	35°19’47’’N	23°57’10’’E	Ph, Chl, Cal, Qz	3.33-3.47			0.44-0.54	41.3 ± 0.6

Petrology and mineral chemistry of additional samples

High-T *Phyllite-Quartzite.* Sample CR1902b was collected in the footwall of the top-to-the-N Cretan detachment. in the northernmost part of the study area. The phyllitic layers alternate with quartz-rich layers and show a blueschist-facies paragenesis with chloritoid + phengite + paragonite + quartz ± apatite ± rutile (Fig. S1a, Table S1). The phyllosilicates define the main foliation, while chloritoid forms syn-kinematic prophyroblasts associated with phengite- and quartz-rich pressure shadows. Pyrophyllite is also locally observed as inclusion in chloritoid. Hematite typically replaces pyrite crystals or forms thin veins that are locally transposed into the main foliation (Fig. S1b). Chemical composition of phengite is relatively homogeneous throughout the sample with a very low Si^{4+} content of 3.08-3.13 apfu and a high muscovite content comprised between 87 and 92 % (Fig. S2, Tables S1, S2). Composition of chloritoid is homogeneous with a low X_{Mg} ratio of 0.10-0.11.

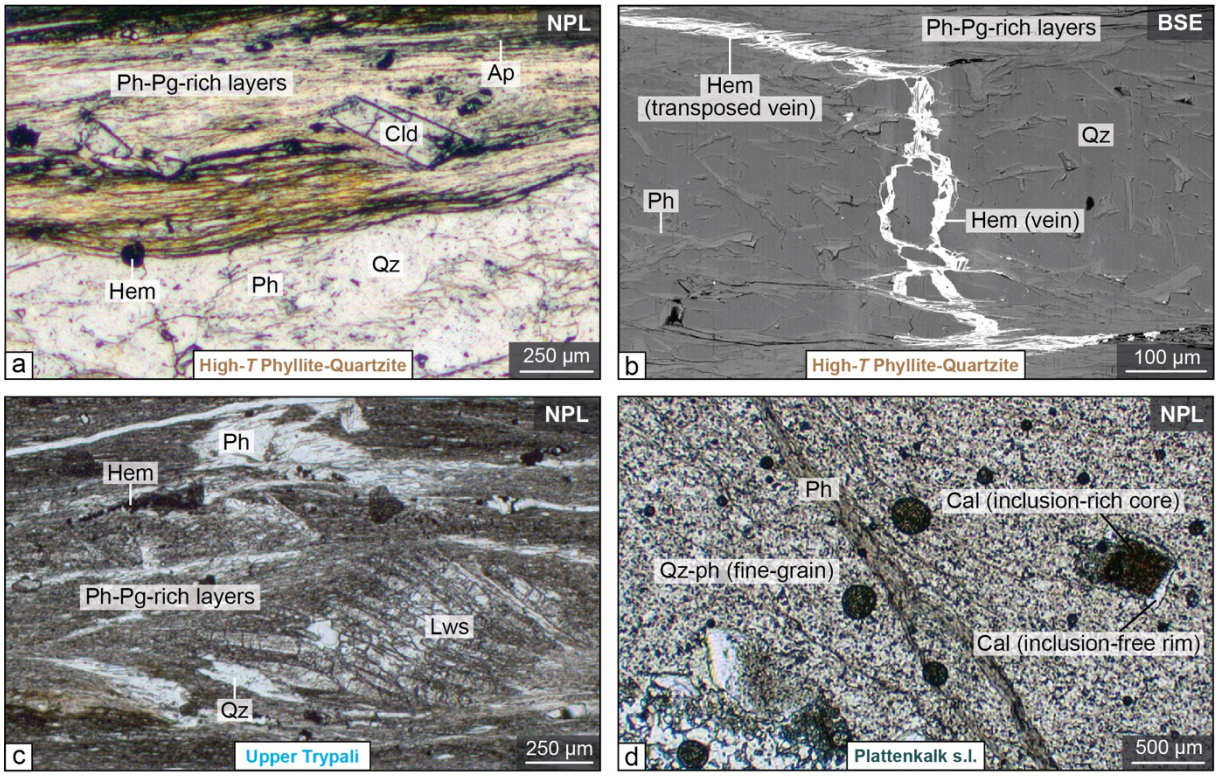

Figure S1: Microscopic observations illustrating the main metamorphic parageneses of additional samples presented in Supporting Information. (**a**) Phyllitic and quartz-rich layers with chloritoid porphyroblasts in a phengite- and paragonite-rich matrix (sample CR1902b). (**b**) Late-stage hematite vein locally transposed into the main foliation defined by phengite and paragonite (sample CR1902b). (**c**) Lawsonite porphyroblasts in phengite- and paragonite-rich layers (sample CR1918a). (**d**) Zoned calcite porphyroblasts in a phengite-quartz-rich matrix with phengite outlining the foliation and oblique C-bands (sample CR2055a). NPL: Non-polarized light. BSE: Backscattered scanning electron microscopy image. Mineral abbreviations are after Whitney and Evans (2010).

Upper Trypali Unit. Sample CR1918a is a phyllite collected in the southwestern part of Crete, from an outcrop also exposing boudinaged marble intercalations. It exhibits a blueschist-facies paragenesis with lawsonite + phengite + paragonite + chlorite + quartz + dolomite ± pyrite ± rutile ± apatite (Fig. S1c, Table S1). The foliation is defined by phengite- and paragonite-rich layers, while lawsonite is aligned or slightly oblique to the stretching direction, forming syn-kinematic prophyroblasts with inclusions outlining the main foliation. Lawsonite is often zoned with a *Ce*-rich core and a *Ca*-rich rim and are sometimes cut by lawsonite-bearing tensile cracks perpendicular to the stretching direction. Phengite

has a moderately variable Si^{4+} content of 3.17-3.24 apfu and a muscovite content typically comprised between 74 and 81 % (Fig. S2, Tables S1, S2). Chlorite consists exclusively of sudoite with a homogeneous X_{Mg} ratio of 0.99-1.00. Pyrite crystals are common but often replaced by hematite.

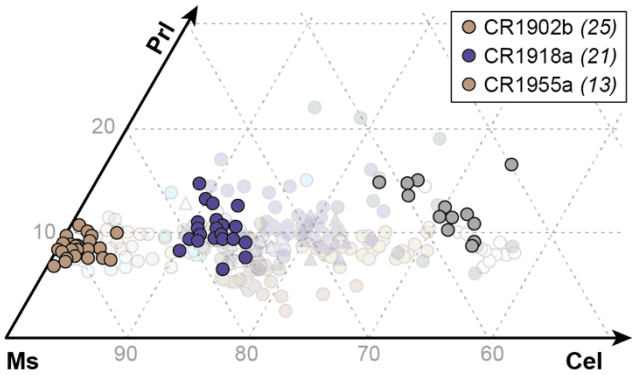

Figure S2: Ternary plot of phengite compositions of additional samples presented in Supporting Information. Symbols in transparency represent the full dataset. The number of electron probe microanalyses is shown in italics.

Plattenkalk s.l. *Unit*. Sample CR2055a is a calcschist interlayered with phyllites from the Gigilos beds that was collected in the eastern part of the study area. The paragenesis consists of zoned-calcite porphyroblasts with inclusion-rich cores in a fine-grained matrix of phengite + quartz + chlorite ± hematite ± titanite ± apatite (Fig. S1d, Table S1). Phengite outlines the foliation and C bands, oblique by about 10° to the main foliation. It has a high and heterogenous Si^{4+} content of 3.33-3.47 and a relatively low muscovite content of 50-61 % (Fig. S2, Tables S1, S2). Chlorite is dominated by clinochlore and chamosite and exhibits a X_{Mg} ratio of 0.44-0.54.

Table S2: Representative probe microanalysis data of key H*P*/L*T* minerals for the additional samples presented in Supporting Information. P-Q: Phyllite-Quartzite.

Mineral	Phengite			Chloritoid	Chlorite	
Unit	High-*T* P-Q	Upper Trypali	Plattenkalk *s.l.*	High-*T* P-Q	Upper Trypali	Plattenkalk *s.l.*
Sample	CR1902b	CR1918a	CR2055a	CR1902b	CR1918a	CR2055a
SiO_2	46.62	48.71	50.40	24.54	36.30	25.60
TiO_2	0.10	0.05	0.11	0.00	0.00	0.05
Al_2O_3	35.93	32.69	27.59	40.16	35.30	20.82
FeO_T	0.59	0.15	2.41	25.81	0.04	24.71
MnO	0.01	0.01	0.07	0.33	0.03	0.17
MgO	0.55	2.34	3.35	1.61	14.40	14.70
CaO	0.01	0.05	0.01	0.01	0.02	0.07
Na_2O	0.84	0.50	0.13	0.00	0.01	0.04
K_2O	9.52	10.16	10.31	0.01	0.42	0.03
Sum	94.19	94.66	94.37	92.55	86.52	86.18
Si	3.10	3.23	3.39	2.04	3.25	2.74
Ti	0.00	0.00	0.01	0.00	0.00	0.00
Al	2.82	2.55	2.19	3.94	3.72	2.63
Fe^{2+}	0.03	0.01	0.14	1.80	0.00	2.21
Fe^{3+}	0.00	0.00	0.00	0.00	0.00	0.00
Mn	0.00	0.00	0.00	0.02	0.00	0.02
Mg	0.05	0.23	0.34	0.20	1.92	2.35
Ca	0.00	0.00	0.00	0.00	0.00	0.00
Na	0.11	0.06	0.02	0.00	0.00	0.00
K	0.81	0.86	0.88	0.00	0.00	0.00

P-T constraints on additional sample

An additional *P-T* pseudosection was calculated for the lawsonite-rich phyllite sample CR1918a, representative of the Upper Trypali Unit (Table S1), following the same approach as for sample CR1965b (see Section 5 in the main text). The model was designed within the chemical system Na_2O-CaO-K_2O-FeO-MgO-Al_2O_3-SiO_2-H_2O-O_2 (NCKFMASHO), using an average bulk composition derived from four SEM surface estimates devoid of carbonate. Due to the lack of robust constraints on the amount of CO_2 in the system, this component was excluded from the thermodynamic calculation. This simplification is justified, as we assume local equilibrium within a microvolume where the observed modal proportion of carbonate is low (<5 %). Fe_2O_3 was considered as negligible due to the low degree of retrogression observed in the analyzed sample. The model was set to 200-450 °C and 0.6-1.8 GPa, assuming water-saturated conditions that are supported by the widespread occurrence of hydrated minerals such as phengite, paragonite, lawsonite and chlorite in the sample.

The best-fit *P-T* conditions cover a large range of pressures (from ~6 to >16 kbar) and temperatures (>230 °C), considering the main paragenesis (Table 1) and the Si^{4+} content in phengite (3.17-3.24 apfu) (Fig. S3). Temperatures can be further constrained, using the RSCM peak metamorphic temperatures obtained for the Upper Trypali Unit (360-390 °C) (Menant *et al.*, this volume). Assuming that the observed mineral assemblage is stable at this peak temperature range, peak metamorphic conditions can be estimated at 8-16 kbar and 360-390 °C. There is also a general agreement between the calculated mineral proportions at 14 kbar, 380 °C and the modal mineral abundance observed in thin section, with the exception of the dolomite and pyrite that were excluded from the pseudosection modeling (compare the two pie charts in Fig. S3).

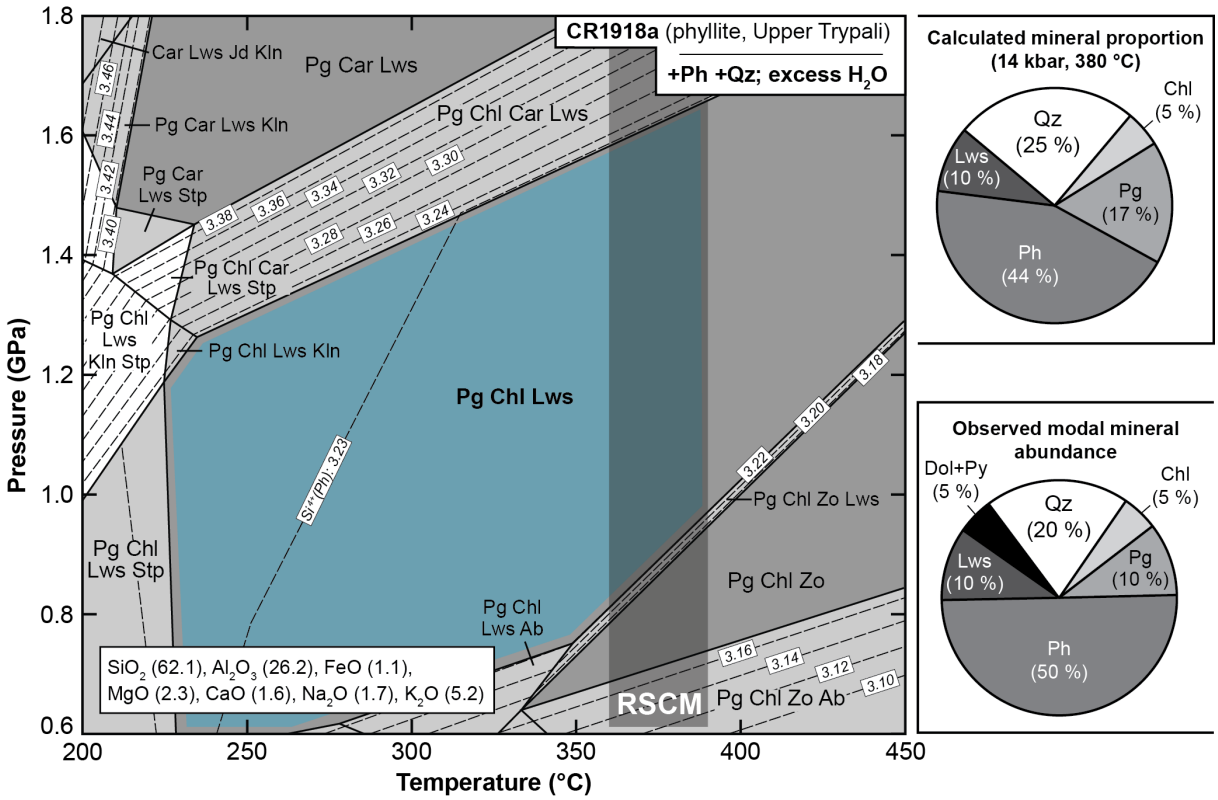

Figure S3: *P-T* pseudosection in the NCKFMASHO system for sample CR1918a (Upper Trypali Unit), highlighting the best-fit area (blue domain) based on observed paragenesis and mineral composition. The RSCM temperature range for this unit is from Menant *et al.* (this volume). Calculated volume proportions and observed modal abundances of the main minerals are represented in insets. Mineral abbreviations are after Whitney and Evans (2010).

Calculated peak metamorphic conditions are globally consistent with previous *P-T* estimates (16-18 kbar, 360-410 °C) (Jolivet *et al.*, 1996), supporting the idea that the Upper Trypali Unit detached from the downgoing slab at a maximum depth of ~55 km. This maximum burial depth is likely smaller than for the overriding Medium-*T* Phyllite-Quartzite Unit that recorded higher peak conditions of 15-17 kbar and 390-440 °C (Figs. 5, 9).

Table S3: Complete *Rb*/*Sr* dataset. Samples with a star (*) are presented in Supporting Information only. MSWD: Mean square weighted deviation.

Sample, material	Rb (ppm)	Sr (ppm)	$^{87}Rb/^{86}Sr$	$^{87}Sr/^{86}Sr$	$^{87}Sr/^{86}Sr$ $2\sigma_m$ (%)
CR2039 (High-*T* Phyllite-Quartzite; **16.4 ± 1.6 Ma**; MSWD = 13; initial $^{87}Sr/^{86}Sr$ = 0.71201 ± 0.00012)					
Apatite	6.01	966.54	0.01799	0.711604	0.0013
Calcite leachate; m@0.8-1.23 A	*n.a.*	*n.a.*	*n.a.*	*n.a.*	*n.a.*
Calcite leachate; nm@1.23 A	*n.a.*	*n.a.*	*n.a.*	*n.a.*	*n.a.*
White mica >180 µm	292.58	128.16	6.60871	0.713503	0.0013
White mica 180-125 µm	298.87	123.84	6.98625	0.713581	0.0029
White mica 125-90 µm	284.52	137.81	5.977	0.713351	0.0009
White mica 90-63 µm	267.14	155.38	4.977	0.713189	0.0016
White mica 90-63 µm (redo)	*n.a.*	*n.a.*	*n.a.*	*n.a.*	*n.a.*
CR1965b (Medium-*T* Phyllite-Quartzite; **20.8 ± 1.4 Ma**; MSWD = 4.1; initial $^{87}Sr/^{86}Sr$ = 0.71137 ± 0.00021)					
Paragonite	141.33	244.69	1.67181	0.712075	0.0012
Chloritoid	39.61	27.69	4.14002	0.712734	0.0023
White mica >160 µm	253.64	100.82	7.28285	0.713712	0.0024
White mica 160-125 µm	265.45	101.28	7.58755	0.713773	0.0015
White mica 125-90 µm	257.89	98.77	7.55856	0.71379	0.0017
White mica 90-63 µm	237.81	90.46	7.61064	0.71381	0.0016
White mica residue (2.5N *HCl*)	39.04	15.56	7.2645	0.713597	0.0015
Calcite with incl. (excluded)	16.77	144.37	0.33628	0.711743	0.0015
Calcite (excluded)	28.64	49.26	1.68281	0.711727	0.0015
Calcite leachate (2.5N *HCL*) (excluded)	13.56	229.38	0.17113	0.711156	0.001
CR1925a (Medium-*T* Phyllite-Quartzite; **24.3 ± 1.2 Ma**; MSWD = 8.1; initial $^{87}Sr/^{86}Sr$ = 0.71073 ± 0.00015)					
Apatite	8.12	202.46	0.11608	0.710818	0.0015
Grey dolomite	11.43	401.8	0.08232	0.710706	0.0011
White mica >125 µm	253.37	64.075	11.44819	0.714587	0.0018
White mica 125-90 µm	254.46	62.29	11.44819	0.714831	0.0024
White mica 90-63 µm	256.04	62.38	11.88309	0.714721	0.0027
Colorless calcite (excluded)	1.46	1211.47	0.00349	0.709282	0.0017
CR1935b (Medium-*T* Phyllite-Quartzite; **15.75 ± 0.55 Ma**; MSWD = 40; initial $^{87}Sr/^{86}Sr$ = 0.71010 ± 0.00094)					
Calcite	0.89	1098.6	0.00235	0.70996	0.0016
Dolomite	9.46	141.62	0.19339	0.710276	0.0014
White mica 250-160 µm	174.74	10.99	46.078	0.720233	0.0011
White mica 160-125 µm	176.44	10.22	50.03	0.721069	0.0017
White mica 125-90 µm	192.34	12.14	45.90317	0.720245	0.0025
White mica >250 µm (excluded)	187.2	12.09	44.84786	0.721043	0.002
CR1920b (Upper Trypali; **19.04 ± 0.76 Ma**; MSWD = 0.62; initial $^{87}Sr/^{86}Sr$ = 0.708335 ± 0.000025)					
Calcite	*n.a.*	*n.a.*	*n.a.*	*n.a.*	*n.a.*
Lawsonite 125-160 µm	*n.a.*	*n.a.*	*n.a.*	*n.a.*	*n.a.*
White mica >160 µm	*n.a.*	*n.a.*	*n.a.*	*n.a.*	*n.a.*
White mica 125-90 µm	*n.a.*	*n.a.*	*n.a.*	*n.a.*	*n.a.*
CR1957b (Upper Trypali; **16.59 ± 0.25 Ma**; MSWD = 0.23; initial $^{87}Sr/^{86}Sr$ = 0.707815 ± 0.000024)					
Calcite I	25.63	4775.88	0.01553	0.707818	0.0006
Calcite II	22.57	3753.07	0.0174	0.70782	0.0011
White mica >125 µm	293.7	75.12	11.31467	0.71042	0.0014
White mica 125-90 µm	290.39	63.62	13.20967	0.710891	0.0033
White mica 90-63 µm	289.7	104.12	8.05162	0.709682	0.0014

Table S3 *(continued)*

Sample, material	Rb (ppm)	Sr (ppm)	$^{87}Rb/^{86}Sr$	$^{87}Sr/^{86}Sr$	$^{87}Sr/^{86}Sr$ $2\sigma_m$ (%)
CR2073 (Upper Trypali; **16.74 ± 0.37 Ma**; MSWD = 5.0; initial $^{87}Sr/^{86}Sr$ = 0.70791 ± 0.00017)					
Apatite	12.64	3669.62	0.00996	0.707881	0.0012
Colorless calcite	4.59	4756.74	0.00279	0.707857	0.001
Grey calcite	6.32	5017.75	0.00364	0.70783	0.001
White mica >125 µm	280.76	28.1	28.93161	0.714866	0.0015
White mica 125-90 µm	296.38	24.74	34.69371	0.71617	0.0022
White mica 90-63 µm	336.68	15.29	63.79	0.722716	0.004
White mica 63-45 µm	345.45	13.87	72.193	0.724643	0.0028
CR1917b (Upper Trypali; **14.66 ± 0.68 Ma**; MSWD = 2.5; initial $^{87}Sr/^{86}Sr$ = 0.708395 ± 0.000041)					
Aragonite	2.18	7210.49	0.00088	0.708402	0.0011
Dolomite	3.32	2637.97	0.00364	0.70835	0.0015
White mica-carpholite	21.46	12.8	4.85169	0.709388	0.0017
White mica 250-160 µm; m@0.84 A	89.24	194.52	1.32743	0.708683	0.002
White mica 160-90 µm; m@0.84 A	60.48	84.11	2.08049	0.70886	0.002
White mica >160 µm; nm@1.22 A	420.63	161.09	7.55605	0.709929	0.0014
White mica 160-90 µm; nm@1.22 A	403.1	157.05	7.42745	0.709916	0.0014
CR1945d (Upper Trypali; **15.5 ± 1.2 Ma**; MSWD = 18; initial $^{87}Sr/^{86}Sr$ = 0.71356 ± 0.00018)					
Dolomite	224.7	48.45	13.4284	0.716466	0.0017
Dolomite leachate (2.5N *HCl*)	208.57	43.06	14.02488	0.716559	0.0007
White mica >125 µm	6.1	301.39	0.05858	0.713474	0.0011
White mica 125-90 µm	10.56	103.13	0.29657	0.713704	0.0017
White mica 90-63 µm	233.5	49.84	13.56662	0.716437	0.0016
White mica-carpholite residue (2.5N *HCL*)	75.94	18.2	12.08242	0.716282	0.0017
CR1945b (vein) (Upper Trypali; **17.02 ± 0.50 Ma**; MSWD = 5.3; initial $^{87}Sr/^{86}Sr$ = 0.713142 ± 0.000073)					
Apatite	1.98	399.25	0.01437	0.713207	0.0018
Dolomite I m@1.23 A	4.09	31.44	0.37681	0.7132	0.0016
Dolomite II m@0.85 A	4.75	116.85	0.1177	0.713138	0.0015
White mica 160-125 µm	287.97	51.3	16.25451	0.717066	0.0017
White mica 125-90 µm	296.44	50.74	16.92	0.717148	0.0019
White mica 90-63 µm	185.16	34.58	15.50781	0.716825	0.0019
CR1945b (host) (Upper Trypali; **16.1 ± 4.6 Ma**; MSWD = 111; initial $^{87}Sr/^{86}Sr$ = 0.71334 ± 0.00059)					
Dolomite	1.42	32.92	0.12519	0.713189	0.0014
Dolomite (Fe) m@0.3 A	2.07	101.67	0.05905	0.71354	0.0019
White mica >160 µm	271.16	54.65	14.36766	0.716628	0.0039
White mica 160-63 µm	219.43	54.03	11.75972	0.715911	0.0019
CR2055b (Plattenkalk s.l.; **41.79 ± 0.66 Ma**; MSWD = 21; initial $^{87}Sr/^{86}Sr$ = 0.7086 ± 0.0011)					
Calcite m@1.23 A	10.65	138.91	0.22194	0.708884	0.0016
Calcite nm@2 A	9.28	217.55	0.12345	0.708583	0.001
White mica 180-125 µm; m@0.85 A	256.77	4.11	182.6219	0.815643	0.004
White mica 125-90 µm; m@0.85 A	256.26	4.14	180.94472	0.813689	0.0042
White mica 90-63 µm; m@0.85 A	231.35	3.74	180.93623	0.815975	0.0024
White mica >125 µm; m@1.23 A	179.02	3.25	160.59892	0.80127	0.0016
White mica 125-90 µm; m@1.23 A	233.26	4.1	166.03349	0.805136	0.0015

Table S3 *(continued)*

Sample, material	Rb (ppm)	Sr (ppm)	$^{87}Rb/^{86}Sr$	$^{87}Sr/^{86}Sr$	$^{87}Sr/^{86}Sr$ $2\sigma_m$ (%)
CR1902b* (High-T Phyllite-Quartzite; **63 ± 20 Ma**; MSWD = 79; initial $^{87}Sr/^{86}Sr$ = 0.71263 ± 0.00055)					
Apatite	50.09	455.65	0.31824	0.71301	0.0013
Chloritoid	11.57	17.53	1.91199	0.714261	0.0021
White mica >160 µm; m@0.85 A	178.98	301.75	1.71707	0.713961	0.0009
White mica 160-90 µm; m@0.85 A	176.15	293.23	1.73907	0.713918	0.0013
White mica >160 µm; nm@1.22 A	206.59	272.69	2.193	0.714805	0.0018
White mica 160-90 µm; nm@1.22 A	205.57	263.6	2.258	0.714756	0.0014
White mica 90-63 µm; nm@1.22 A	192.57	226.42	2.46242	0.714722	0.0018
CR1918a* (Upper Trypali; **31.9 ± 3.3 Ma**; MSWD = 9.5; initial $^{87}Sr/^{86}Sr$ = 0.70821 ± 0.00010)					
Lawsonite m@2.2 A	*n.a.*	*n.a.*	*n.a.*	*n.a.*	*n.a.*
Lawsonite nm@2.2 A	*n.a.*	*n.a.*	*n.a.*	*n.a.*	*n.a.*
White mica nm@2.2 A	*n.a.*	*n.a.*	*n.a.*	*n.a.*	*n.a.*
White mica >200 µm	*n.a.*	*n.a.*	*n.a.*	*n.a.*	*n.a.*
White mica 200-125 µm	*n.a.*	*n.a.*	*n.a.*	*n.a.*	*n.a.*
White mica 125-90 µm	*n.a.*	*n.a.*	*n.a.*	*n.a.*	*n.a.*
CR2055a* (Plattenkalk s.l.; **41.3 ± 0.6 Ma/37.1 ± 0.6 Ma**)					
Calcite	*n.a.*	*n.a.*	*n.a.*	*n.a.*	*n.a.*
White mica >200 µm	*n.a.*	*n.a.*	*n.a.*	*n.a.*	*n.a.*
White mica 200-90 µm	*n.a.*	*n.a.*	*n.a.*	*n.a.*	*n.a.*

Rb/Sr-dating results on additional samples

In the High-*T* Phyllite-Quartzite Unit, a chloritoid-bearing phyllite (sample CR1902b; Fig. S1a) shows clear isotopic disequilibrium, yielding a meaningless age of 63 ± 20 Ma with a high mean squared weighted deviation (MSWD = 79; Fig. S4a). This disequilibrium is evident in the heterogenous isotopic composition of the five white-mica fractions that reveals multiple generations of white micas that were not distinguishable by chemical analysis (Fig. S3). The occurrence of late-stage hematite veins that are locally transposed into the main foliation suggests the infiltration of oxidizing fluids under a ductile-brittle regime that may have reacted with muscovite (Fig. S1b), offering an explanation for the observed isotopic disequilibrium. This unreliable age is not discussed further.

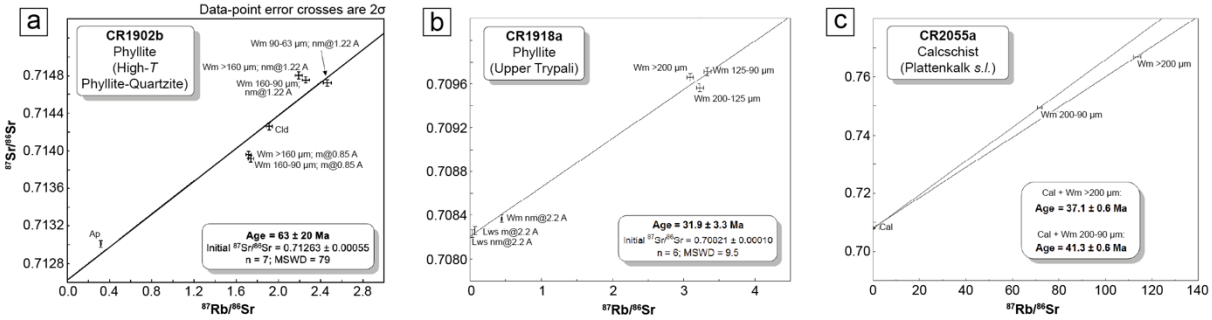

Figure S4: (**a-c**) Rb/Sr isochron diagrams for the additional samples presented in Supporting Information. MSWD: Mean square weighted deviation. Mineral abbreviations are after Whitney and Evans (2010).

In the Upper Trypali Unit, a lawsonite-bearing phyllite (sample CR1918a; Fig. S1c) yields a six-point isochron including lawsonite that corresponds to a questionable age of 31.9 ± 3.3 Ma (MSWD = 9.5; Fig. S4b). The moderate scatter of the three radiogenic ^{87}Sr-rich white-mica fractions explains the high MSWD and age uncertainty and may indicate multiple generations of white micas with a distinct isotopic signature, supported by the moderately variable composition of phengite (Fig. S2, Table S1). Accordingly, this likely unreliable age reflects an inherited isotopic signature, similarly to some K/Ar ages on white micas (Seidel *et al.*, 1982) and a K/Ar age cluster of 37-40 Ma from fault gouges (Ring *et al.*, 2022) that are consistently interpreted as mixing ages.

A calcschist belonging to the Gigilos beds that is part of the Plattenkalk *s.l.* Unit (sample CR2055a; Fig. S1d) yields two two-point isochrons that correspond to ages of 41.3 ± 0.6 Ma and 37.1 ± 0.6 Ma (Fig. S4c). These poorly constrained ages are, however, supported by the apparently well-defined age of 41.79 ± 0.66 Ma (MSWD = 21; Fig. 6l) obtained on another sample collected from the same outcrop. These dating may indicate either an early tectono-metamorphic event preserved in this siliciclastic formation, or an inherited isotopic signature, and therefore meaningless ages, as shown by zoned calcite and variable phengite composition (Figs. S1d and S3; see also Section 8.2 in the main text).

Description of analyzed samples for (U-Th-Sm)/He thermochronology

Sample CR2062 is a coarse-grained quartzite from the High-*T* Phyllite-Quartzite Unit (Table S4). It is composed of poorly to moderately flattened quartz porphyroclasts, typically a few hundred-µm size, set in a fine-grained matrix of quartz and phengite (Fig. S5a). Zircon is occasionally observed in thin section. Partly dissolved grain boundaries of quartz porphyroclasts, along with dark seams that define a weak foliation, indicate widespread dissolution-precipitation processes. Additionally, quartz porphyroclasts exhibit weak undulose extinction indicating minor intracrystalline plastic deformation.

Table S4: Analyzed samples for (U-Th-Sm)/He thermochronology. Further details on the thermochronological results are provided in Table 3. Age with an asterisk (*) has been obtained after data curation (see Section 8.3 in the main text).

Sample	Tectono-metamorphic unit	Latitude	Longitude	Elevation (m)	Mean ZHe age (Ma)
CR2062	High-*T* Phyllite-Quartzite	35°24’19’’N	23°44’01’’E	508	14.8 ± 2.2
CR2066	Medium-*T* Phyllite-Quartzite	35°20’45’’N	23°40’01’’E	590	11.7 ± 1.3
CR2069	Medium-*T* Phyllite-Quartzite	35°18’43’’N	23°42’23’’E	345	12.5 ± 1.3*
CR2044	Medium-*T* Phyllite-Quartzite	35°16’52’’N	23°43’28’’E	556	14.0 ± 1.2

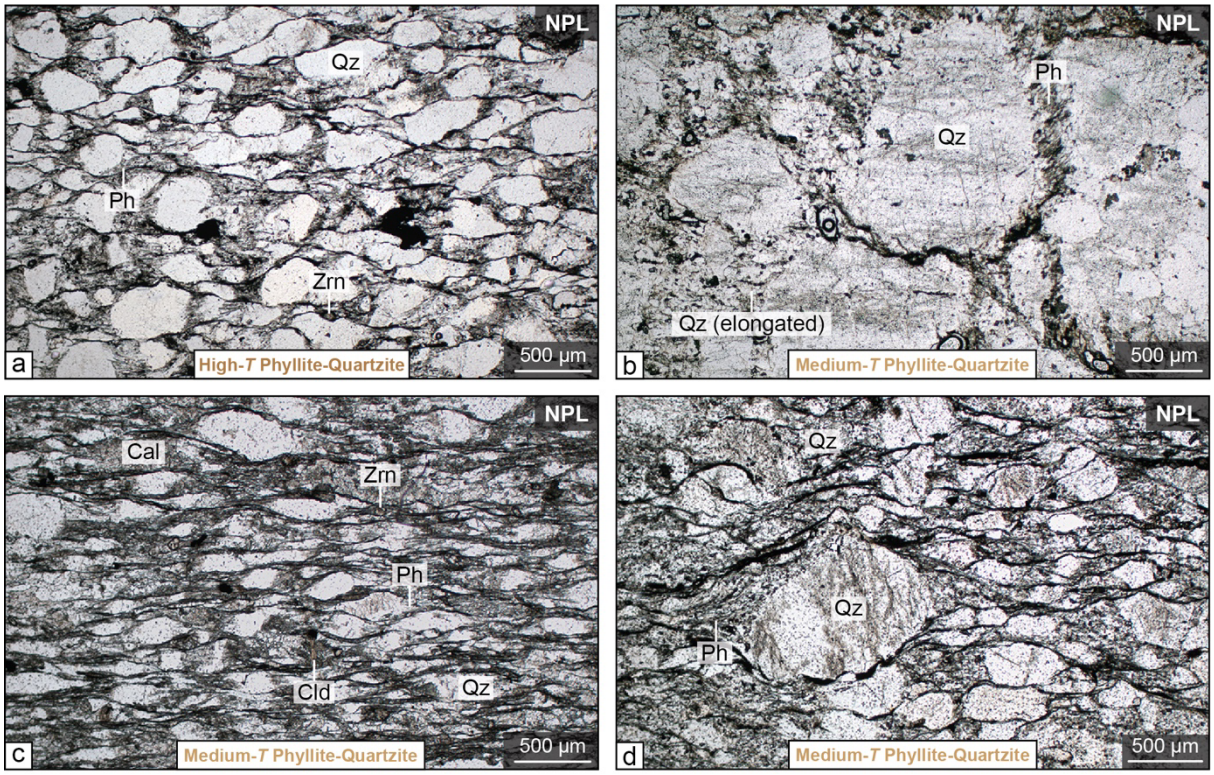

Figure S5: Microscopic observations illustrating the mineral composition and microstructures of analyzed samples for (U-Th-Sm)/He thermochronology. (**a**) Poorly to moderately deformed quartz porphyroclasts in a fine-grained matrix of quartz and phengite (sample CR2062). (**b**) Poorly deformed quartz porphyroclasts in a fine-grained matrix of elongated quartz and phengite (sample CR2066). (**c**) Moderately deformed calcite and quartz porphyroclasts associated with chloritoids in a fine-grained matrix of quartz, phengite and chlorite (sample CR2069). (**d**) Poorly to moderately deformed quartz porphyroclasts in a fine-grained matrix of quartz and phengite (sample CR2044). NPL: Non-polarized light. Mineral abbreviations are after Whitney and Evans (2010).

Sample CR2066 is a coarse-grained quartzite from the Medium-*T* Phyllite-Quartzite Unit (Table S4). It is composed of quartz porphyroclasts, typically a few hundred-µm to mm size, set in a fine-grained matrix of elongated quartz and phengite defining a hardly visible foliation (Fig. S5b). Partly dissolved grain boundaries of quartz porphyroclasts indicate dissolution-precipitation processes. Additionally, quartz porphyroclasts exhibit weak undulose extinction indicating minor intracrystalline plastic deformation.

Sample CR2069 is a coarse-grained quartzite from the Medium-*T* Phyllite-Quartzite Unit (Table S4). It is composed of moderately flattened quartz and calcite porphyroclasts, typically a few hundred-µm to mm size, associated with chloritoid forming radiating aggregates (Fig. S5c). The surrounded fine-grained matrix is made of quartz, phengite and minor chlorite. Zircon is occasionally observed in thin section. Partly dissolved grain boundaries of quartz and calcite porphyroclasts, along with dark seams that form a well-defined foliation, indicate widespread dissolution-precipitation processes. Additionally, quartz porphyroclasts exhibit weak undulose extinction indicating minor intracrystalline plastic deformation.

Sample CR2044 is a coarse-grained quartzite from the Medium-*T* Phyllite-Quartzite Unit (Table S4). It is composed of poorly to moderately flattened quartz porphyroclasts, typically a few hundred-µm to mm size, set in a fine-grained matrix of quartz and phengite (Fig. S5d). Partly dissolved grain boundaries of quartz porphyroclasts, along with dark seams that define a weak foliation, indicate widespread dissolution-precipitation processes. Additionally, quartz porphyroclasts exhibit weak undulose extinction indicating minor intracrystalline plastic deformation.

References

Jolivet, L., Goffé, B., Monié, P., Truffert-Luxey, C., Patriat, M. and Bonneau, M. (1996) Miocene detachment in Crete and exhumation P-T-t paths of high-pressure metamorphic rocks, *Tectonics*, 15(6), pp. 1129–1153. https://doi.org/10.1029/96TC01417.

Menant, A., Augier, R., Bessière, E., Glodny, J., Angiboust, S., Jolivet, L. and Oncken, O. (this volume) Setting the cadence of slicing events along deep subduction interfaces: 1. The tectonic and thermal structure of the high-*P* duplex in western Crete (Hellenic margin), *Tektonika*.

Ring, U., Fassoulas, C., Uysal, I.T., Bolhar, R., Tong, K. and Todd, A. (2022) Nappe Imbrication Within the Phyllite-Quartzite Unit of West Crete: Implications for Sustained High-Pressure Metamorphism in the Hellenide Subduction Orogen, Greece, *Tectonics*, 41(11). https://doi.org/10.1029/2022TC007430.

Seidel, E., Kreuzer, H. and Harre, W. (1982) A late Oligocene/early Miocene high pressure belt in the external Hellenides, *Geol. Jahrb., Reihe E*, 23, pp. 165–206.

Whitney, D.L. and Evans, B.W. (2010) Abbreviations for names of rock-forming minerals, *American Mineralogist*, 95(1), pp. 185–187. https://doi.org/10.2138/am.2010.3371.